

RESEARCH ARTICLE



Label-free identification and chemical characterisation of single extracellular vesicles and lipoproteins by synchronous Rayleigh and Raman scattering

Agustin Enciso-Martinez ^a, Edwin Van Der Pol ^{b,c,d}, Chi M. Hau ^{c,d}, Rienk Nieuwland ^{c,d},
Ton G. Van Leeuwen ^{b,d}, Leon W.M.M. Terstappen ^a and Cees Otto ^a

^aDepartment of Medical Cell BioPhysics, TechMed Centre, University of Twente, Enschede, The Netherlands; ^bDepartment of Biomedical Engineering and Physics, University of Amsterdam, Amsterdam, The Netherlands; ^cLaboratory Experimental Clinical Chemistry, University of Amsterdam, Amsterdam, The Netherlands; ^dVesicle Observation Center, Amsterdam University Medical Centers, Location AMC, University of Amsterdam, The Netherlands

ABSTRACT

Extracellular vesicles (EVs) present in blood originate from cells of different origins such as red blood cells (RBCs), platelets and leukocytes. In patients with cancer, a small portion of EVs originate from tumour cells and their load is associated with poor clinical outcome. Identification of these tumour-derived extracellular vesicles (tdEVs) is difficult as they are outnumbered by EVs of different tissue of origin as well as a large number of lipoproteins (LPs) that are in the same size range. In order to detect tdEVs from the abundant presence of other particles, single-particle techniques are necessary. Here, synchronous Rayleigh and Raman scattering is used for that purpose. This combination of light scattering techniques identifies optically trapped single particles based on Rayleigh scattering and distinguishes differences in chemical composition of particle populations based on Raman scattering. Here, we show that tdEVs can be distinguished from RBC EVs and LPs in a label-free manner and directly in suspension.

ARTICLE HISTORY

Received 13 December 2019
Revised 30 January 2020
Accepted 11 February 2020



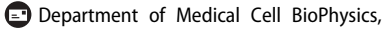
KEYWORDS


Extracellular vesicles; lipoproteins; optical trapping; Rayleigh scattering; Raman scattering; label-free; single particle

Introduction

Extracellular vesicles (EVs) are spherical particles enclosed by a lipid membrane that are released by prokaryotic and eukaryotic cells. EVs play a key role in intercellular communication [1], that enables cells to send and receive messages encoded in the biomolecules that make up the EVs, namely lipids, proteins, nucleic acids and sugars. In recent years, it has become widely accepted that body fluids, such as blood, urine and cerebrospinal fluid, contain EVs [2]. Under physiological conditions, blood contains 10^6 – 10^{12} EVs per mL [2–4], which originate from blood cells and the vessel wall [5]. However, in pathological conditions, for example, cancer cells may release EVs. Hence, in cancer, tumour-derived EVs (tdEVs) may be present within the circulation [6–8]. In peripheral blood, the concentration of tdEVs, as identified after EpCAM enrichment and using cytokeratin immunofluorescent staining, ranges from 10 to 10^3 EVs per mL and is strongly associated with poor clinical outcome [8–11]. In these studies, only the larger tdEVs were identified and new studies are still needed to determine the frequency and characteristics of the smaller tdEVs. In addition, characterisation of the composition of tdEVs may contain information to determine the optimal therapy.

Isolating, identifying and characterising tdEVs is challenging due to the (1) heterogeneity of EVs, (2) limited knowledge on the chemical composition of EVs, (3) low light scattering efficiency, and (4) size overlap between EVs and non-EV particles, such as lipoproteins (LPs). The smallest EVs range in diameter from 30 to 50 nm, depending on the sample, whereas the largest EVs exceed 1 μm [4,12–14]. These small size ranges together with a refractive index (RI) below typically 1.42 make that EVs scatter light inefficiently. In addition, EV isolation methods lack standardisation and the study of EVs can be biased depending on the isolation method used [15,16]. Therefore, isolation methods that avoid altering the physical and chemical properties of EVs are preferred. Specific labelling of tdEVs is particularly relevant for blood plasma samples, where tdEVs are outnumbered by LPs [2,11]. Although size exclusion chromatography (SEC) based on CL-2B can efficiently remove small LPs (\sim <70 nm) [17], bigger LPs in the size range of EVs, such as very low-density lipoproteins (VLDL) and chylomicrons (CM), remain present. Bulk analysis methods, such as Western blot and mass spectroscopy, are useful to characterise the EV composition in a label-free manner, but not at the single-particle level. The inherent averaging of bulk

CONTACT Agustin Enciso-Martinez  a.encisomartinez@utwente.nl; Cees Otto  c.otto@utwente.nl 

 Supplemental data for this article can be accessed [here](#).

© 2020 The Author(s). Published by Informa UK Limited, trading as Taylor & Francis Group on behalf of The International Society for Extracellular Vesicles. This is an Open Access article distributed under the terms of the Creative Commons Attribution-NonCommercial License (<http://creativecommons.org/licenses/by-nc/4.0/>), which permits unrestricted non-commercial use, distribution, and reproduction in any medium, provided the original work is properly cited.

particle analysis methods precludes the detection of rare EV populations, such as tdEVs. Therefore, a technique that can identify and characterise single tdEVs is an important step to exploit tdEVs as biomarker for cancer.

Detection of single EVs by elastic light scattering has been proven to be a feasible approach [18–20]. The light that illuminates a particle is partially scattered with the same energy as the incident light, a phenomenon known as Rayleigh scattering. In addition to Rayleigh scattering, light can also be scattered inelastically, after which the light is shifted in frequency. The shifts in frequency will become visible when a monochromatic laser source is used for illumination. The spectrum resulting from this so-called Raman scattering directly depends on the molecules that the particle is composed of. Hence, Raman scattering provides information about the chemical composition of the EVs. The scattered light can be collected and even the light scattered by single EVs can be detected [20]. Furthermore, if the laser illuminating a particle is tightly focused, the particle near the focus will experience a net force directing it to the axial centre of the laser beam where the particle remains optically trapped as long as the laser is on [20–28]. Synchronised Rayleigh and Raman scattering of optically trapped single particles enables single-particle label-free analysis [20].

Here, we hypothesise and show that single EVs from different cellular origin are characterised by a different Raman spectrum in dependence of their variation in molecular composition. Furthermore, we will show that LP particles can be distinguished from EVs directly in suspension without labelling. As a proof of principle, we show here label-free differentiation of single red blood cell (RBC) EVs, LPs and prostate cancer EVs in plasma.

Materials and methods

Tumour-derived EVs

The two prostate cancer cell lines PC-3 and LNCaP American Type Culture Collection (ATCC, CRL-1435 and CRL-1740, USA) were used as a model to produce tdEVs. Both cell lines were cultured at 37°C and 5% CO₂ in RPMI-1640 with L-glutamine medium (Lonza, Cat. No.: 12-702 F) supplemented with 10% (v/v) foetal bovine serum (FBS), 10 units/mL penicillin and 10 µg/mL streptomycin. The initial cell density was 10,000 cells/cm² as recommended by the ATCC. Medium was refreshed every second day. At 80–90% confluence, cells were washed three times with phosphate-buffered solution (PBS) and cultured in FBS-free RPMI-1640 with L-glutamine medium (Lonza, Basel, Switzerland, Cat. No.: 12-702 F) supplemented with 1 unit/mL penicillin

and 1 µg/mL streptomycin. After 2–3 days of cell culture, cell supernatant was collected in a 15 mL tube (Cellstar® tubes, Greiner Bio-one BV, Alphen a/d Rijn, The Netherlands) and centrifuged at 500–800 xg at room temperature for 10 min (Centrifuge 5804, Eppendorf, Hamburg, Germany). The pellet containing dead or apoptotic cells and large cell fragments was discarded. The collected supernatants containing PC-3 and LNCaP EVs were stored in aliquots at –80°C. Samples were thawed in a water bath at 37°C before use. EV size distribution and concentration were determined by both nanoparticle tracking analysis (NTA) (NanoSight NS500, UK) and flow cytometry (SI).

Red blood cell (RBC) derived EVs

RBC EVs were obtained from a RBC concentrate (150 mL, Sanquin Bloodbank, Amsterdam, The Netherlands) and diluted 1:1 with filtered PBS. Samples were centrifuged three times at 1560 xg for 20 min at 20°C using a Rotina 46RS centrifuge (Hettich, Tuttlingen, Germany). The EV-containing supernatant was pooled and deposited in aliquots of 50 µL, which were snap frozen in N₂ (l) for 15 min and stored at –80°C until use. Samples were thawed in a water bath at 37°C before use. EV size distribution and concentration were determined by both NTA (NanoSight NS500, UK) and flow cytometry (SI).

“Platelet particles”

With the term “platelet particles”, we refer to platelet-derived EVs and LP particles present in platelet concentrate, which can be optically trapped (*vide infra*). Platelet concentrate (100 mL, Sanquin Bloodbank, Amsterdam, The Netherlands) was diluted 1:1 with filtered PBS. Next, 40 mL acid citrate dextrose (ACD; 0.85 mol/L trisodium citrate, 0.11 M D-glucose and 0.071 M citric acid) was added and the suspension was centrifuged for 20 min at 800 xg, 20°C. Thereafter, the supernatant was centrifuged (20 min at 1560 xg, 20°C). This centrifugation procedure was repeated twice to ensure removal of platelets. The supernatant was pooled and deposited in aliquots of 50 µL, which were snap frozen in N₂ (l) for 15 min and stored at –80°C until use. Samples were thawed in a water bath at 37°C before use. Particle size distribution and concentration were determined by both NTA (NanoSight NS500, UK) and flow cytometry (SI).

Plasma

Blood from anonymous healthy donors was obtained from the TNW-ECTM-donor services (University of

Twente, Enschede, The Netherlands) after written informed consent. The blood sample was collected by venipuncture in CellSave preservative tubes (10 mL, Menarini – Silicon Biosystems Inc, Huntington Valley, PA, USA). Blood was centrifuged (Centrifuge 5804, Eppendorf, Hamburg, Germany) in a CellSearch conical tube for 10 min at 800 xg without brake (on deceleration). Plasma was taken up to 1 cm above the RBC layer and stored in 1.5 mL tubes (Greiner Bio-one, Alphen a/d Rijn, The Netherlands, Cat.No.: 616,201) at -80°C until use. The particle size distribution and concentration were determined by flow cytometry (SI) only, due to the small sample availability. With the term “plasma particles”, we refer to all particles present in plasma, including EVs and LPs.

Lipoprotein particles (LPs)

From all types of LP particles, we expect that our Raman setup, flow cytometer and NTA primarily measure chylomicrons (CM) and very low-density lipoproteins (VLDL). Therefore, we acquired CM from human plasma (Sigma-Aldrich Chemie N.V., The Netherlands, SRP6304) with a purity of $\geq 95\%$ (SDS-PAGE), as specified by the provider. VLDL from human plasma were acquired (Sigma-Aldrich Chemie N.V., The Netherlands, 437,647) with a purity of $\geq 95\%$ of total LP content by electrophoresis, as specified by the provider.

Nanoparticle tracking analysis (NTA)

All samples except plasma (due to limited sample availability) were characterised with NTA (NanoSight NS500, Malvern, UK) to confirm the presence of submicrometer particles and obtain an order of magnitude estimate of the concentration of particles exceeding the minimum detectable size. For EVs, the minimum detectable diameter of the used instrument is 70–90 nm [14]. For detailed NTA settings see SI.

Flow cytometry (FCM)

To confirm the presence of EVs and LPs, FCM (A60-Micro, Apogee, UK; Rosetta Calibration, Exometry, The Netherlands) was performed on all the samples. In short, we triggered on side scattering using a threshold of 14 arbitrary units, corresponding to a side scattering cross-section of $\sim 10 \text{ nm}^2$ (Rosetta Calibration, Exometry, The Netherlands). The flow rate was $3.01 \mu\text{L}/\text{min}$. To calibrate the side scattering detector, Rosetta Calibration was applied [29], which assumes that EVs are core-shell particles with a 5 nm thick shell of RI $n_{\text{shell}} = 1.48$ and a core of RI $n_{\text{core}} = 1.40$. Two μm APC Quantitative (Q-APC) beads (BD Biosciences, San Jose, CA, USA) and SPHERO™ PE MESF beads (Spherotech Inc., Illinois, USA) were used to calibrate the fluorescence detectors. We applied the flow-cytometry scatter ratio (Flow-SR) to determine the effective RI [19], allowing differentiation between LPs and EVs [30]. Table 1 of this manuscript reports the *Concentration FCM total*, *Concentration FCM RI<1.42*, *Concentration FCM RI>1.45*, and *Concentration FCM labelled EVs*. *Concentration FCM total* are all detected particles exceeding the side scattering cross-section of $\sim 10 \text{ nm}^2$. Assuming that EVs match the aforementioned RI distribution, this corresponds to EVs of 162 nm and larger in diameter. *Concentration FCM RI<1.42* are all detected particles for which Flow-SR can be applied (200–800 nm in diameter and ~ 1 order of magnitude above the detection limits for forward and side scatter) and which have a RI<1.42. As previously confirmed [19,30], most of these particles are EVs. *Concentration FCM RI>1.45* are all detected particles for which Flow-SR can be applied (200–800 nm in diameter and ~ 1 order of magnitude above the detection limits for forward and side scatter) and which have a RI>1.45. As previously confirmed [19,30], most of these particles are LPs. Gates are shown in Figure S5.

Sample preparation

In synchronised Rayleigh and Raman scattering, the PC-3 EVs, LNCaP EVs, RBC EVs, “platelet particles”

Table 1. Sample pre-characterisation by NTA and FCM. Particle sample concentrations (C_p) as given by NTA (Concentration NTA) and FCM (concentration FCM total). Concentration FCM RI<1.42 are all detected particles between 200 and 800 nm in diameter and ~ 1 order of magnitude above the detection limits for forward and side scatter, and which have an RI <1.42. Concentration FCM RI>1.45 are all detected particles between 200 and 800 nm in diameter and ~ 1 order of magnitude above the detection limits for forward and side scatter, and which have an RI >1.45. ^aValue missing due to limited sample availability.

	Concentration NTA (mL^{-1})	Concentration FCM total (mL^{-1})	Concentration FCM RI<1.42 (mL^{-1})	Concentration FCM RI>1.45 (mL^{-1})
PC-3 EVs	1.9×10^9	3.8×10^8	6.5×10^7	9.1×10^5
LNCaP EVs	1.1×10^9	6.8×10^8	9.5×10^7	4.4×10^6
RBC EVs	4.3×10^{10}	4.1×10^9	3×10^9	1.1×10^9
“Platelet particles”	8.4×10^{10}	2.3×10^{10}	1.9×10^{10}	3.7×10^9
“Plasma particles”	NA ^a	1.6×10^{11}	2×10^{10}	7.7×10^9

and “plasma particles” were, if necessary, diluted in PBS up to a concentration of $\sim 10^{10}$ particles/mL. A 50 μL suspension of each particle type was placed on a well glass slide (BMS Microscopes; 1.0–1.2 mm thick, Cat. No.: 12,290). The sample was covered with a glass cover slip (VWR Ltd, thickness No. 1, diameter: 22 mm, Cat. no.: 631–0158) and sealed with glue (EVO-STIK, Impact) onto the well glass slide to avoid evaporation [20]. The glue was then cured at room temperature for ~ 30 min. The closed well glass slide was placed under the microscope objective of the Rayleigh–Raman spectrometer.

Optical setup and measurements

The Rayleigh–Raman spectrometer is based on a homebuilt Raman spectrometer integrated with the base of an upright optical microscope (Olympus BX41). A single laser beam from a Coherent Innova 70 C laser ($\lambda_{\text{exc}} = 647.089$ nm) was used for illuminating and trapping particles [20]. Rayleigh and Raman scattering were collected with a cover glass corrected dry objective (Olympus, 40x, NA: 0.95), separated in a homebuilt spectrometer and simultaneously detected with a single CCD camera (Andor Newton DU-970-BV). The spectrometer had an average dispersion of ~ 2.3 cm^{-1} (0.11 nm) wavenumber per pixel over the CCD camera surface with 1600 pixels along the dispersive axis and 200 pixels along the other axis. The spectral resolution was ~ 3.0 cm^{-1} . For further details about the Rayleigh–Raman spectrometer see SI. The laser power was measured underneath the objective and adjusted to 70 mW. By moving the objective along the z-axis, the laser focal spot is focused inside the solution, ~ 37 μm below the cover slip. The focal spot has a theoretical diameter of 0.4 μm and a Rayleigh range of 1.2 μm based on full width half maximum. 256 Rayleigh–Raman spectra were acquired with an acquisition time of 38 ms each over a period of 9.7 s. The trapped particles were then released from the optical trap by blocking the laser beam with a shutter for 1 s. This measurement cycle was repeated 100 times, which resulted in $100 \times 256 = 25,600$ Rayleigh–Raman spectra per measurement. In total, we characterised 481 individual particles.

Data analysis

Calibration

The intensity and wavelength of the Rayleigh–Raman spectrometer was calibrated to convert the raw, measured data from pixels vs relative counts to calibrated data in wavenumber (cm^{-1}) vs counts. The pixel-to-wavenumber

conversion was performed with a Raman spectrum from toluene, which has peaks of known relative wavenumber shift with respect to the exciting laser line at 0 cm^{-1} shift, and an argon-mercury lamp with narrow emission lines known with picometre accuracy. The wavelength-dependent transmission of the setup and the pixel-to-pixel variation in the detection sensitivity of the CCD camera was corrected with an intensity calibration. This intensity calibration was performed by acquisition of a white light spectrum from a tungsten halogen light source (AvaLight-Hal; Avantes BV, Apeldoorn, The Netherlands) that results in the light detection efficiency for the entire setup per pixel. The offset of the detector depends on the detector parameters and was obtained from a measurement without any light falling onto the detector. The spectrum of the entire light path through the setup with the laser on, but without a sample, was acquired to determine the background spectrum, which was subtracted from the measured data. All software was developed in-house with MATLAB (2017b).

Time traces

The Rayleigh–Raman spectra comprised a dataset composed of 25,600 spectra per measurement of 100 cycles. Rayleigh time traces were obtained by integrating the Rayleigh band, centred between -33 and 58 cm^{-1} . The Raman time traces resulted from integrating a lipid-protein Raman band from 2811 to 3023 cm^{-1} . The Rayleigh and Raman bands were localised and integrated using the trapezoidal method with unit spacing. Before the integration of the lipid-protein Raman band, singular value decomposition (SVD) was performed on the Raman spectra to improve the signal-to-noise ratio [31,32]. The first 32 S-components were selected for reconstruction of the data. The integrated Rayleigh and Raman values of each cycle were concatenated and plotted versus time, allowing the selection of time intervals of interest.

Segmentation of time traces

The Rayleigh scattering time traces were used to identify the time intervals corresponding to single trapping events. Single trapping events are visualised as step-wise increases in the Rayleigh signal [20]. These steps were manually segmented and their time intervals were used to select the corresponding Raman spectra. A Raman spectrum of a single particle was thus acquired as the average Raman spectrum during the length of one step. All the molecules in the Raman focal spot contribute to the Raman spectra. However, we are only interested in the contribution of a single particle in the focal spot and not the background. Hence, to account for any background contribution (e.g.

water or soluble particles), the immediate previous segment to the step was also segmented and the corresponding Raman spectrum was used for background subtraction by a linear least-squares (LLS) fit. All software was developed in-house with MATLAB (2017b).

Backscattering calculations

To assess the diameter range of the optically trapped particles, we compared the measured and theoretical backscattering intensities. To calibrate the backscattering intensities, we related the measured backscattering intensities of polystyrene beads (PS) (Nanosphere; Thermo Fisher, Waltham, MA, USA) with mean diameters of 100, 125, 147, 296 and 799 nm to their theoretical backscattering cross-section by least square fitting. Theoretical backscattering cross-sections were calculated as a function of particle diameter with step sizes of 10 nm using the Mie theory scripts of Mätzler [33] in MATLAB (2018b) and incorporating the particle diameter and RI, RI of the medium, the numerical aperture of the microscope objective (NA = 0.95) and the wavelength (647.1 nm), polarisation and intensity of light. Details, equations and limitations of the applied model are extensively described and published [29]. Note that we let the optical axis of the microscope objective overlap with the negative z-axis of the Cartesian coordinate system, as defined in Figure 3 of de Rond et al. [29], and that the integral of equation 4 [29] was numerically solved in 24 steps for both the azimuthal and polar angles. We assumed a RI of 1.586 for polystyrene [34] and 1.464 for silica [35]. Silica beads (Si) (Silica Kisker, Steinfurt, Germany) were used to validate our model for particles with a lower RI than PS. Because EVs have a low (<1.42) but heterogeneous RI [30], they were modelled as a core-shell particle with the core containing predominantly water ($n_{\text{H}_2\text{O}} = 1.33$) and dissolved biological molecules, together giving rise to a lower and upper boundary core RI $n_{\text{coreLower}} = 1.36$ and $n_{\text{coreUpper}} = 1.40$, respectively; a shell consisting mostly of lipid molecules ($n_{\text{lipids}} = 1.49$) and embedded proteins ($n_{\text{protein}} = 1.44$), together giving rise to a shell RI $n_{\text{shell}} = 1.48$ with a thickness of 6 nm.

Multivariate analysis

Following the segmentation of the time traces and background subtraction by LLS fit, the full dataset comprised a total of 481 Raman spectra corresponding to 481 individual particles: PC-3 EVs ($n = 94$), LNCaP EVs ($n = 75$), RBCs EVs ($n = 56$), “platelet particles” ($n = 103$) and “plasma particles” ($n = 153$). The mean Raman spectra per sample type were computed for spectral comparison. The Raman spectrum of each particle was interpolated to the same wavenumber axis and baseline correction and de-

noising were performed on the full dataset using a function called BEADS [36]. The cut-off frequency used was 0.006 cycles/sample, a regularisation parameter of 0.0050, 0.0500 and 0.0400, a first-order filter and an asymmetry ratio of 6. Next, each Raman spectrum was normalised to have a mean of zero and a standard deviation of one. Finally, principal component analysis (PCA) was performed on the mean centred data in the spectral regions 800–1780 cm^{-1} and 2800–3080 cm^{-1} . Data analysis was performed using MATLAB (2017b) and Eigenvector (Eigenvector Research, Inc., Washington, US) software.

Results

Pre-characterisation of samples by NTA and flow cytometry

Table 1 shows the particle concentration as measured by NTA and FCM. The particle distributions from NTA confirmed that the majority of particles have a size range smaller than 600 nm (SI). The estimated concentrations are 10^9 tDEVs per mL and 10^{10} RBC EVs and “platelet particles” per mL. In addition, assuming a RI < 1.42 for EVs, FCM confirmed the presence of mainly EVs in the PC-3, LNCaP and RBC samples. EVs and LPs were present in both the plasma and platelet concentrate samples, assuming a RI < 1.42 for EVs and RI > 1.45 for LPs.

Detection of single EVs

We start by demonstrating trapping and detection by synchronous Rayleigh–Raman scattering of single EVs [20] originating from different cells and LPs. Figure 1(a,b) show the Rayleigh and Raman scattering signals of multiple trapping cycles during 900 s corresponding to LNCaP and RBC EVs, respectively. Rayleigh time traces of the rest of the samples are shown in Figure S6. The laser beam is unblocked and blocked at the start and end of a cycle of 9.7 s. Although not shown in the time traces, the laser remains blocked for 1 s between cycles to enable enough time for the particles to be released from the focal spot. The associated Raman scattering signals were obtained from the integration of the lipid-protein band (2811–3023 cm^{-1}) in the Raman spectrum. Because the Rayleigh scattering signal is much more intense than the Raman scattering signal, optical trapping can be much better studied using the Rayleigh signal. The Raman signals, on the other hand, contain information about the chemical composition of the trapped particles. Figure 1(a,b) show a clear correlation between Rayleigh and Raman

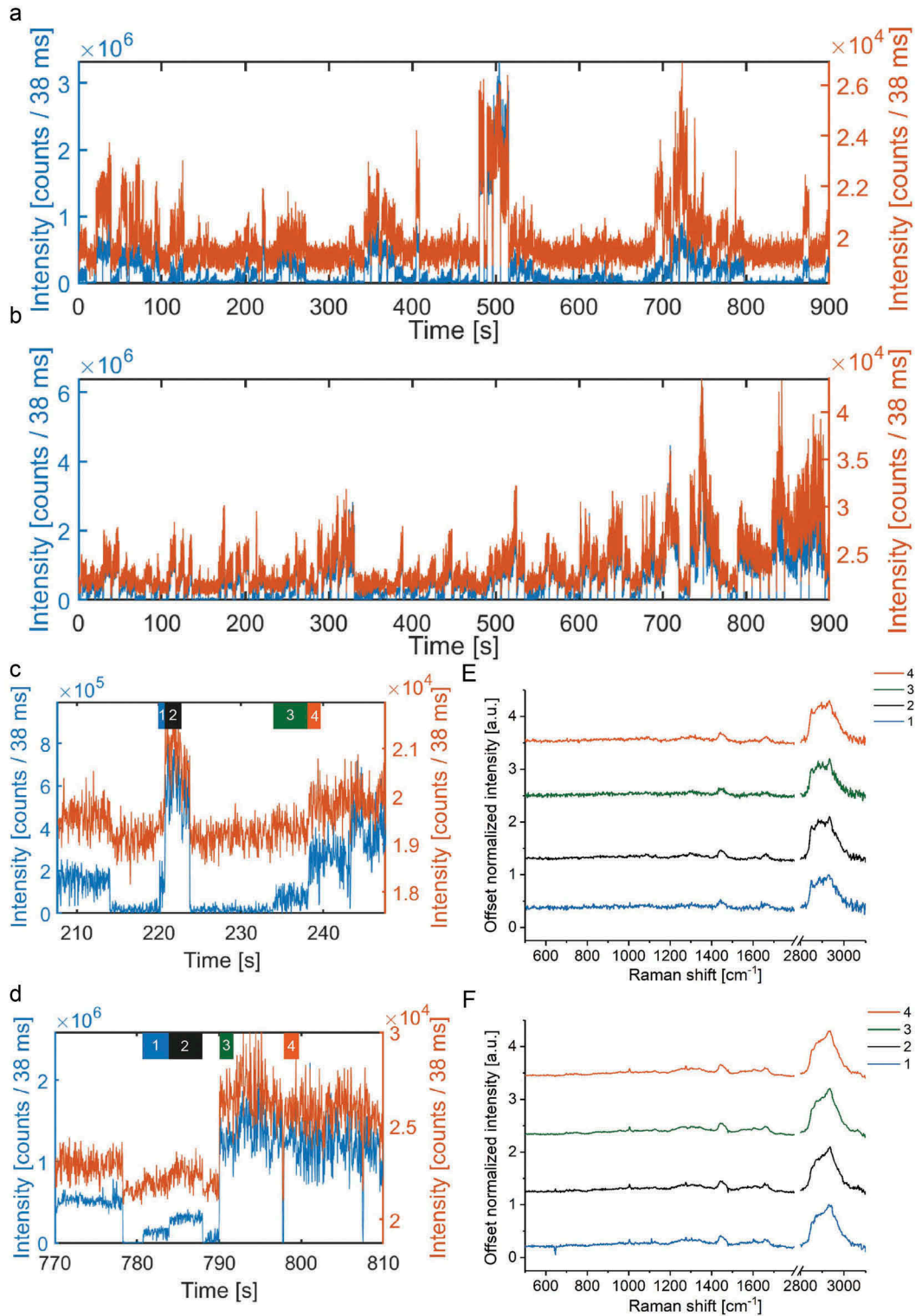


Figure 1. Synchronous intensity time traces of Rayleigh (blue) and Raman (orange) scattering signals from (a) LNCaP EVs and (b) RBC EVs, resulting from peak integration of the Rayleigh peak located between -33 and 58 cm^{-1} and a lipid-protein band between 2811 and 3023 cm^{-1} . (a) and (b) are a concatenation of multiple cycles of Rayleigh and Raman scattering signals with an integration time of 38 ms and a cycle duration of 9.7 s. (c) and (d) show a magnification of (a) and (b), respectively, indicating four time intervals (labels at the top of the plots) corresponding to the trapping of (c) single LNCaP EVs and (d) single RBC EVs. (e) and (f) display Raman spectra of single LNCaP and RBC EVs, respectively. The colour-coded Raman spectra in (e) and (f) correspond to the 4 time points in (c) and (d), respectively.

signal pairs for each sample, with cross-correlation coefficients of 0.81 for the LNCaP EVs and 0.93 for the RBC EVs. The cross-correlation coefficients for PC-3, plasma and platelet time traces are 0.92, 0.82, 0.87, respectively.

When plotted on 40 s intervals, it becomes apparent that the Rayleigh scattering signals show discrete steps in time [Figure 1\(a,b\)](#), which indicates single trapping events. Thus, the Rayleigh scattering signal can be used to define the time intervals for extraction of the Raman spectrum corresponding to a single particle. In [Figure 1\(c,d\)](#), we labelled four trapping events. Whereas each step is caused by a single particle entering the focal spot, only the first step corresponds to a time interval where only 1 particle is present in the focal spot. [Figure 1\(e,f\)](#) shows the background corrected Raman spectra corresponding to the numbered time traces in [Figure 1\(c,d\)](#), respectively. The lipid-protein band ($2811\text{--}3023\text{ cm}^{-1}$) has higher intensity than the Raman bands in the fingerprint region ($500\text{--}1800\text{ cm}^{-1}$) and spectral differences are visible between LNCaP EVs ([Figure 1\(e\)](#)) and RBC EVs ([Figure 1\(f\)](#)).

Spectral characterisation of various EVs types and LPs

To differentiate EVs from other particles, such as LPs, and to identify EVs of different cellular origin, we segmented single particle trapping events from the Rayleigh time traces and obtained the time intervals where individual EVs contributed to a Raman spectrum. The mean Raman spectra after baseline correction and noise removal are shown in [Figure 2\(a\)](#) for 56 individual RBC EVs, 94 PC-3 EVs, 75 LNCaP EVs, 153 “plasma particles” and 103 “platelet particles”. The mean Raman spectra of all EV types show lipid and protein bands at 1126 , $1297\text{--}1303$, $1441\text{--}1443$, $1655\text{--}1659$, and $2811\text{--}3030\text{ cm}^{-1}$. PC-3 and LNCaP EVs have a similar mean Raman spectrum (cross-correlation coefficient of 0.996). RBCs, PC-3 and LNCaP EVs show corresponding bands at 1004 , 1340 , $1607\text{--}1609\text{ cm}^{-1}$ and a higher protein-to-lipid ratio than “plasma particles” and “platelet particles”. “Plasma particles” and “platelet particles” share a similar spectral profile, as quantified by a cross-correlation coefficient of 0.997. The mean Raman spectra of PC-3 and LNCaP EVs show peaks specific to this type of EVs: $1243\text{--}1245$ (Amide III [37]), $1321\text{--}1323$ (guanine [37]), 1663 (Amide I [37]), among others. In addition, the protein marker band at 1004 cm^{-1} from the amino acid phenylalanine is clearly visible in all EV types but not in the “plasma particles” and “platelet particles”.

The spectral differences between the various particle types can be further detailed by principal component analysis (PCA), which discloses the main sources of spectral variation in the data set comprising 481 individual particles. [Figure 2\(c\)](#) shows two principal component loadings (PC1 and PC2) that together account for 73.7% of the variance in the full dataset. PC1 shows more lipid features than PC2, which in turn displays more protein features. [Figure 2\(b\)](#) depicts a scatter plot in which each dot represents a single particle with a certain value for PC1 and PC2. Particles with similar scores for principle components have similar Raman spectra (and similar chemical content) and are clustered together. The higher the score value of a particle for a principal component, the larger the contribution of that principal component.

When plotting the scores values of PC1 against PC2, three main clusters can be identified: 1) RBC EVs, 2) PC-3 and LNCaP EVs (tdEVs) and 3) “plasma particles” and “platelet particles”. The ellipses around each particle type represent the 95% confidence interval. The results show that EVs can be distinguished from particles present in the plasma and platelet samples. Furthermore, tdEVs can be distinguished from RBC EVs. Most of the EVs are negative for PC1 ([Figure 2\(b\)](#)), while most of the “platelet particles” and “plasma particles” are positive for PC1, which indicates that there is a larger protein contribution for EVs than for “platelet particles” and “plasma particles”. In addition, most of the “plasma particles” and “platelet particles” show a very similar Raman profile and they fall in the same cluster. In [Figure 2\(b\)](#), most of the “plasma particles” and “platelet particles” are positive for PC1 and negative or close to zero for PC2, which indicates that these particles have a high PC1 contribution, which mainly shows a lipid profile. These loadings suggest that the trapped events in RBC, PC-3, LNCaP are EVs, whereas the trapped events in plasma and platelet concentrates are LPs. To verify that most of the particles in our plasma and platelet samples are LPs, we performed Raman spectroscopy on commercially available LPs. [Figure 3](#) shows that the mean Raman spectra of CM and VLDL shows a lipid profile highly similar to “plasma particles” and “platelet particles”. Hence, the abundance of trapped “plasma particles” and “platelet particles” are indeed LPs, and those LPs can be clearly differentiated from EVs without labelling based on their chemical composition.

EV size estimation based on Rayleigh scattering

To establish a relationship between the measured Rayleigh scattering intensity of the optically trapped particles and their diameter, [Figure 4](#) shows the Rayleigh scattering

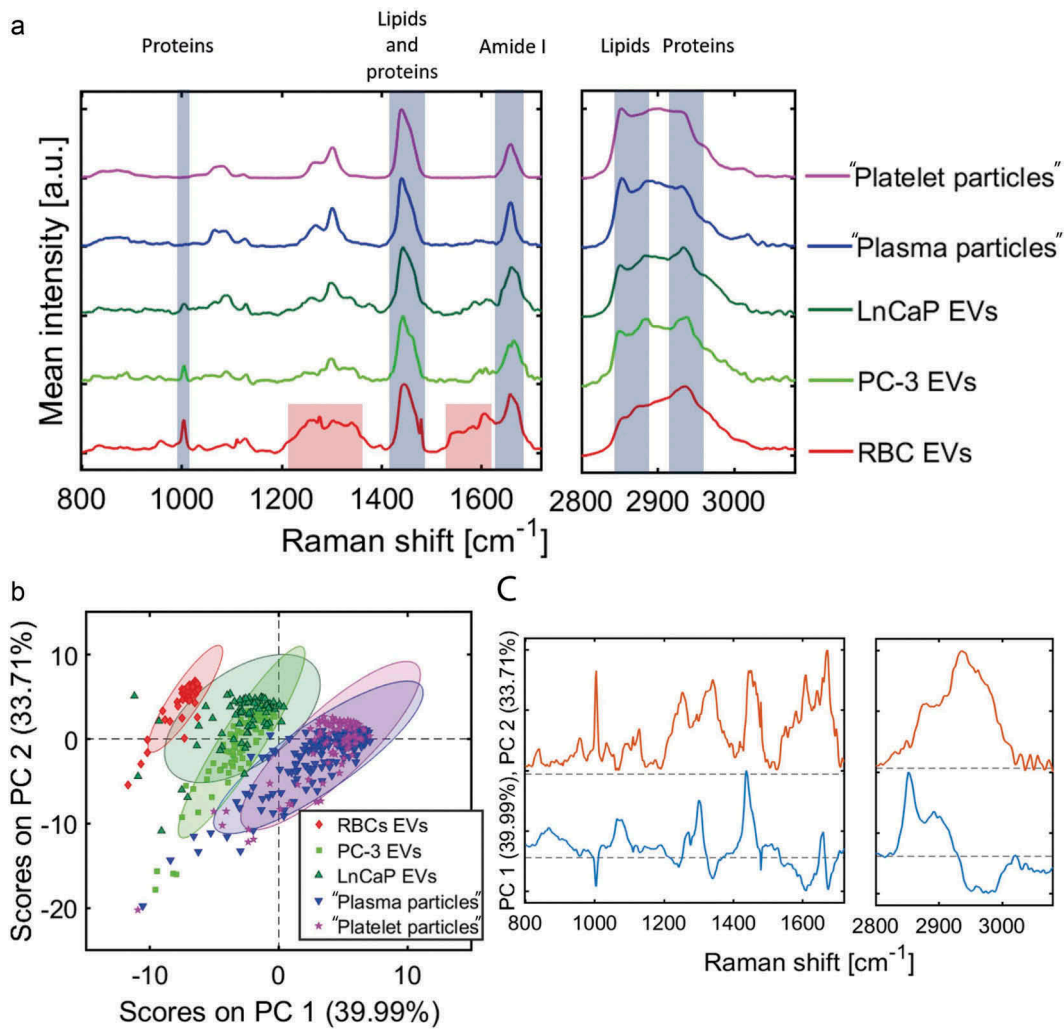


Figure 2. Principal component analysis of EVs. (a) Mean Raman spectra of single RBCs EVs ($n = 56$), PC-3 EVs ($n = 94$), LNCaP EVs ($n = 75$), "plasma particles" ($n = 153$) and "platelet particles" ($n = 103$) displaying common Raman bands to all EV types: 1298–1300 (CH_2), 1442 (lipids and proteins), 1656 (Amide I), 2811–3023 (lipids and proteins) cm^{-1} . (b) First and second principal component scores. Ellipse represents the 95% confidence interval. (c) First two principal component loadings resulting from PCA analysis on the dataset of 481 single particles. The cumulative variance of these loadings represents 73.7%. The largest spectral variations are at the following locations: 1004, 1301, 1437, 1443, 1445, 1479, 1609, 1659, 1671, 2850, 2883, and 2933 cm^{-1} .

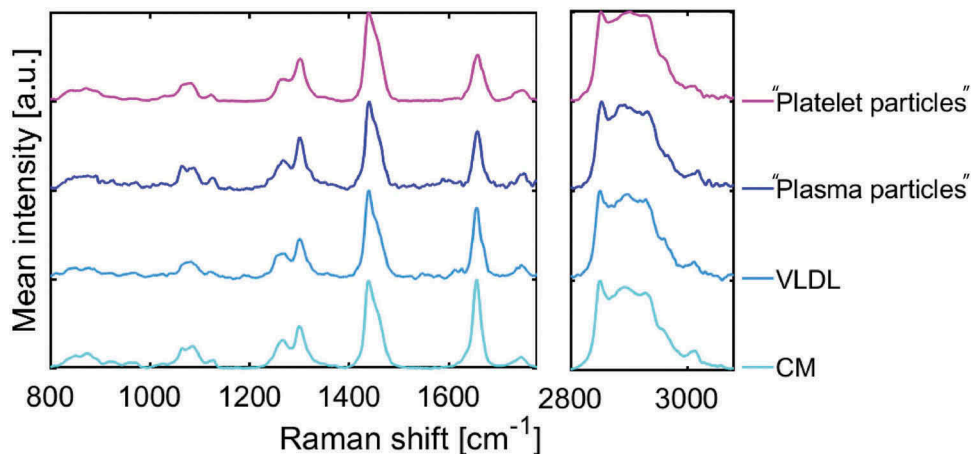


Figure 3. Normalised mean Raman spectra of CM ($n = 98$), VLDL ($n = 118$), "plasma particles" ($n = 153$) and "platelet particles" ($n = 103$). Baseline and noise removal were performed on each individual Raman spectrum belonging to a single particle.

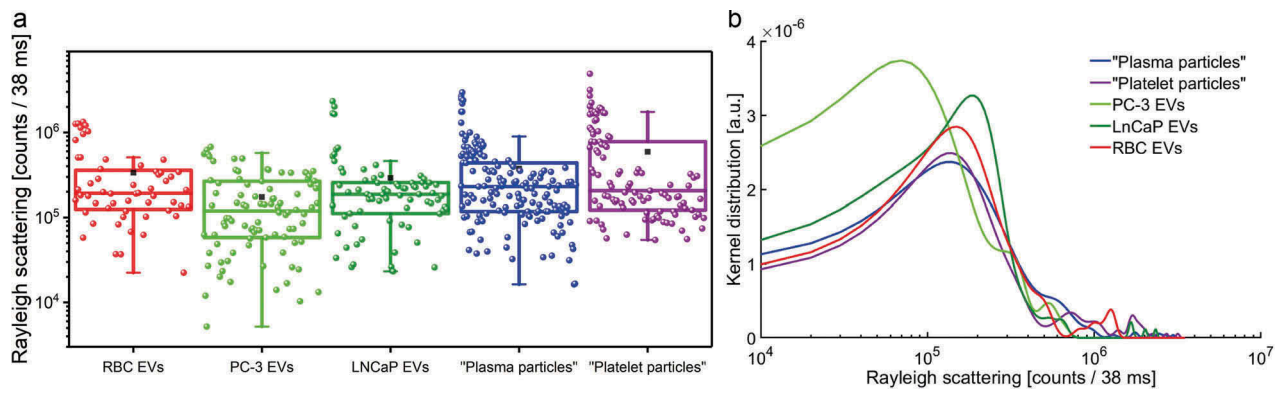


Figure 4. Rayleigh scattering distributions. (a) The boxplots (dots represent single particles) show the Rayleigh scattering distributions for RBC EVs, LNCaP EVs, PC-3 EVs, “plasma particles” and “platelet particles”. The boxes range from the 25th percentile to the 75th percentile, which corresponds to the interquartile range (IQR). The mean is indicated by the black squares. The whiskers range are within $1.5 \times$ IQR. (b) Kernel distribution of the Rayleigh scattering intensity of single EVs and non-EV particles.

distribution from single trapped LNCaP EVs, PC-3 EVs, RBC EVs, “plasma particles” and “platelet particles”. Panel A shows that the interquartile range (IQR) for all the particle types is overlapping and the spread of plasma and platelet particles is larger than that of the EV types. The Rayleigh values for PC-3 and LNCaP EVs mainly overlap and the spread marked by the whiskers is between 5.2×10^3 and 5.7×10^5 . Because the Rayleigh scattering distribution does not follow a normal distribution, a non-parametric distribution (kernel distribution) was fitted to the density function of the Rayleigh scattering values of single particles (Figure 4(b)).

Next, we calibrated the measured Rayleigh scattering intensities with a Mie scattering model by using PS beads with an RI of 1.586. With calibration, we mean that we related the measured backscattering intensity in arbitrary units to the theoretical scattering cross-section in nm^2 . Next, Si beads were used to validate the model for particles with a lower RI than PS. The collection of light in the backscatter direction causes sharp oscillations, which are somewhat smoothed by averaging over the finite collection angle of the microscope objective. The theoretically determined backscattering cross-section is the cross-section related to the scattering of light towards the objective ($\text{NA} = 0.95$) (Figure 5, left axis). The experimentally obtained backscatter intensity (data points in Figure 5(a), right axis) of PS and Si beads is in agreement with the Mie calculations ($R^2 = 0.999$). The green curves in Figure 5(a,b) depict the simulated backscattering cross-sections (left axis) and thus the corresponding backscattering intensity (right axis) from EVs. Despite the small RI difference between EVs ($n_{\text{core}} \approx 1.37$) [38] and water ($n = 1.33$), we show that sub-micrometre EVs exceed the detection limit of our instrument (black line in Figure 5(b)) by measuring and calibrating the Rayleigh backscattering intensity. Hence, the measured Rayleigh backscattering intensity

enables to select the Raman scattering intensities of individually trapped EVs in the sub-micrometre range. It can be noticed that for particles with diameters above 200 nm the Rayleigh scattering of EVs is much lower than for PS or Si beads, which can be related to the molecular composition and density of molecules of EVs.

The oscillatory behaviour of the Mie curves as a function of particle size (green curves in Figure 5) precludes that a unique solution of the size of the EVs can be extracted based on the measured Rayleigh backscattering (grey area in Figure 5(a)). However, we can estimate the size range of the particles that are optically trapped. For instance, the grey area in Figure 5(a) corresponds to the Rayleigh scattering values of all EVs with a median value of 1.87×10^5 counts/38 ms and mean lower and upper boundaries (whiskers in Figure 4(a)) of 1.7×10^4 and 5.14×10^5 , respectively. The black line in Figure 5(b) indicates the detection limit of the Rayleigh scattering based on the lowest Rayleigh intensity corresponding to a visible trapping event (lowest whisker in Figure 4(a)). Thus, the estimated diameter range of the smallest detectable EVs is between 80 to 320 nm.

Discussion

The identification and phenotyping of single and rare EVs in plasma, such as tdEVs, is challenging due to (1) their overlap in size with other biological nanoparticles, specially LPs and platelets, (2) the low number of EV surface antigens that are available for antibody labelling, and (3) the lack of chemical characterisation methods at the single EV level [2,39,40]. Previously, we showed the trapping of single EVs in suspension, identified those single trapping events by triggering on Rayleigh scattering and, synchronously, obtained their chemical composition by Raman scattering [20].

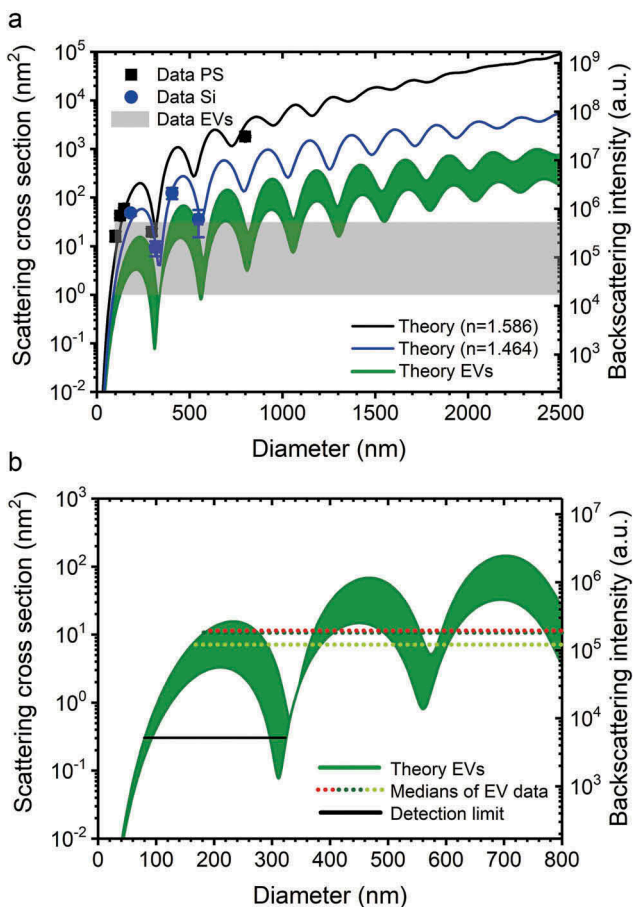


Figure 5. (a) Prediction of the back-scattered signals (lines) for linearly polarised light at a wavelength 647.1 nm from a PS beads (black), Si beads (blue) and EVs (green) using Mie theory. The left vertical axis depicts the cross-section integrated over the backscattering angles with an NA of 0.95. The right vertical axis depicts the counts per 38 ms measured on PS beads (back squares) and Si beads (blue dots). Vertical error bars indicate the SD of measured amplitudes and horizontal error bars are SD of size distributions as provided by manufacturer. The refractive indices used to model the particles were: Ps = 1.586, Si = 1.464, $EV_{core} = 1.36$ and $EV_{shell} = 1.48$ (lower boundary), $EV_{core} = 1.40$ and $EV_{shell} = 1.48$ (upper boundary) with a shell thickness of 6 nm for lower and upper boundaries. The grey area corresponds to the Rayleigh scattering intensity range from PC-3, LNCaP and RBC EVs in Figure 4(a), with upper and lower boundaries that correspond to the mean value of the upper and lower whiskers. (b) Magnification of (a) showing the median Rayleigh scattering values for RBC EVs (red), LNCaP EVs (dark green) and PC-3 EVs (light green). The detection limit (black line) corresponds to the lowest whisker value in Figure 4(a), which is for PC-3 EVs.

In this study, we showed that synchronous Rayleigh–Raman scattering of optically trapped particles enables to differentiate single EVs from LPs and to differentiate tdEVs from RBC EVs without labelling. The samples in our study were also characterised with NTA and FCM.

Here, tdEVs were represented by EVs derived from prostate cancer cell lines. It is assumed that all particles from LNCaP and PC-3 are tdEVs and all particles from RBC concentrate are EVs. By synchronous acquisition of both Rayleigh and Raman scattering, we trapped single particles and disclosed their chemical fingerprint.

The identification of individual particles was enabled by a short acquisition time (38 ms) and triggering on Rayleigh scattering. Rayleigh scattering is much more intense than the Raman scattering, which allowed identification of small particles that are not visible in the Raman time traces. Hence, the Rayleigh time traces show clearer steps when a particle is trapped. Examples of intensity difference in Rayleigh and Raman scattering are shown in Figure 1(c,d), before step 3 and from steps 1 to 2, respectively. Here, the Rayleigh signal shows clear steps, which are absent or not clear in the Raman signal. The Raman time traces result from the integration of the lipid-protein band (2811–3023 cm⁻¹), which is the highest intensity Raman band for EVs and LPs.

The experimental identification of single vs. multiple nanoparticles depends to a great extent on the particle concentration. Hence, two strategies can be followed to avoid trapping of multiple particles regarded as one: (1) dilute the suspension of particles and (2) decrease the illumination time. Dilution aims at decreasing the probability of trapping multiple particles during the integration time by a reduction of the concentration and given the stochastic nature of the trapping process. However, the time required to measure a statistical significant number of particles increases, lowering the throughput of the technique. Decreasing the illumination time enables time traces of higher temporal resolution, allowing a better distinction of particles entering the focal spot, but decreasing the signal-to-noise ratio. In this study, we chose a trade-off between concentration of particles and illumination time. The highest concentration of particles we measured was $C_p = 4.25 \times 10^{10}$ particles/mL (NTA) for the RBC EVs. With an estimated microscopic focal volume of 1.82 fl using the Rayleigh criterion, the number of particles in the focal volume when the laser is blocked is approximately 0.0774. For the RBC EV sample, the time trace contains segments that change more gradually as compared to a less-concentrated sample like PC-3 EVs (Figure 1(a,b)). The gradual change is caused by the rapid accumulation of particles in the trap, making it difficult to distinguish and segment single trapping events and decreasing the

amount of Raman spectra per particle, hence decreasing the signal-to-noise-ratio. Therefore, we used concentrations equal or lower than C_p .

The hereby presented method enabled the label-free distinction of tdEVs, i.e. PC-3 and LNCaP, from RBC EVs and LPs in plasma and platelet concentrates with a 95% confidence interval (Figure 2(b)). The Raman spectra of EVs show a larger contribution of proteins compared to LPs. For instance, phenylalanine is clearly visible in EVs (1004 cm^{-1}) while not detected in LPs. In addition, the lipid-protein band ($2811\text{--}3023\text{ cm}^{-1}$) shows a higher protein contribution for EVs than for LPs. PCA suggested that most of the particles trapped in plasma and platelet concentrates are LPs. To further verify this, we compared the Raman fingerprint of the trapped LPs with commercially available LPs isolated by electrophoresis (Figure 3). The Raman spectra of the particles trapped in plasma and platelet concentrates correlates with the one measured on the commercial LPs and with [41]. We mainly measure LPs in plasma, which agrees with previous studies that estimate the LP frequency in plasma to be much larger than the EV frequency [2].

The difference between tdEVs and RBC EVs may come from the presence of derivatives of haemoglobin [42]. PC-3 and LNCaP EVs are not distinguished from each other and two possible explanations are that the chemical differences among these EVs derived from prostate cancer cells is too small to detect, or there is a high heterogeneity within each EV type, which has been previously suggested [25].

The size of the trapped particles can be estimated by Mie theory based on the Rayleigh scattering. Rayleigh scattering depends on size and RI of the particles. It is known that the particle size distribution of EVs in body fluids are not normally distributed. Hence, the Rayleigh scattered light by EVs in blood will also not have a normal distribution. Indeed, the Rayleigh distributions of Figure 4 reveal a lognormal distribution, rather than a normal distribution. By comparing the EV values for the Rayleigh backscattering cross-section with the Mie model in Figure 5, it was estimated that the lowest size range of particles probed is between 80 and 320 nm. Detecting smaller particles is challenging because their signal is overwhelmed by the background noise (S7). The NTA distributions (S1–S4) suggest that the size range of the trapped EVs corresponds with the range up to 600 nm in the Mie model (Figure 5).

The label-free and non-destructive Rayleigh–Raman method allows identification and differentiation of single EVs from LPs, and tdEVs from RBC EVs. Additional Raman and Rayleigh analysis discloses the chemical composition of particles and estimates their size range. The data suggests that the origin of single particles present in plasma can be traced based on their unique Raman molecular fingerprint. Hence, the label-free method of

synchronous Rayleigh and Raman provides a way to verify the nature of EVs and other particles in body fluids for diagnostic and prognostic purposes.

Acknowledgments

The authors thank Aufried T.M. Lenferink from the Department of Medical Cell BioPhysics, University of Twente, Enschede, The Netherlands, for excellent support during the Raman measurements and Leonie de Rond from the Department of Biomedical Engineering and Physics, Amsterdam UMC, University of Amsterdam, Amsterdam, The Netherlands for measuring the FCM data of RBC and platelet samples.

Disclosure of interest

The authors report no conflict of interest.

Funding

This work is part of the Perspectief Program Cancer ID [14193], which is in part financed by the Netherlands Organization for Scientific Research–Domain Applied and Engineering Sciences (NWO-TTW). Part of this work was supported by the VENI program [15924, E. van der Pol] of the Netherlands Organization for Scientific Research–Domain Applied and Engineering Sciences (NWO-TTW).

ORCID

Agustin Enciso-Martinez  <http://orcid.org/0000-0002-9856-9160>

Edwin Van Der Pol  <http://orcid.org/0000-0002-9497-8426>

Rienk Nieuwland  <http://orcid.org/0000-0002-5394-2152>

Ton G. Van Leeuwen  <http://orcid.org/0000-0002-5642-1133>

Leon W.M.M. Terstappen  <http://orcid.org/0000-0001-5944-3787>

Cees Otto  <http://orcid.org/0000-0001-6955-4843>

References

- [1] Kanada M, Bachmann MH, Contag CH. Signaling by extracellular vesicles advances cancer hallmarks. [Internet]. *Trends Cancer*. 2016;21:84–94.
- [2] Johnsen KB, Gudbergsson JM, Andresen TL, et al. What is the blood concentration of extracellular vesicles? Implications for the use of extracellular vesicles as blood-borne biomarkers of cancer. *Biochim Biophys Acta Rev Cancer*. [Internet]. 2019;1871(1),109–116. Available from: <https://linkinghub.elsevier.com/retrieve/pii/S0304419X1830180X>
- [3] van der Pol E, Böing AN, Harrison P, et al. Classification, functions, and clinical relevance of extracellular vesicles. *Pharmacol Rev*. [Internet]. 64 (3),676–705 (2012). Available from: <http://www.ncbi.nlm.nih.gov/pubmed/22722893>

- [4] Arraud N, Linares R, Tan S, et al. Extracellular vesicles from blood plasma: determination of their morphology, size, phenotype and concentration. *J Thromb Haemost.* [Internet]. 2014;12(5):614–627. Available from: <http://www.ncbi.nlm.nih.gov/pubmed/24618123>
- [5] Berckmans RJ, Nieuwland R, Böing AN, et al. Cell-derived microparticles circulate in healthy humans and support low grade thrombin generation. *Thromb Haemost.* [Internet]. 2001;85(4):639–646. Available from: <http://www.ncbi.nlm.nih.gov/pubmed/11341498>
- [6] Zwicker JI, Liebman HA, Neuberger D, et al. Tumor-derived tissue factor-bearing microparticles are associated with venous thromboembolic events in malignancy. *Clin Cancer Res.* [Internet]. 2009;15(22):6830–6840. Available from: <http://clincancerres.aacrjournals.org/cgi/doi/10.1158/1078-0432.CCR-09-0371>
- [7] Li J, Sherman-Baust CA, Tsai-Turton M, et al. Claudin-containing exosomes in the peripheral circulation of women with ovarian cancer. *BMC Cancer.* [Internet]. 2009;9(1), 244. Available from: <http://bmccancer.biomedcentral.com/articles/10.1186/1471-2407-9-244>
- [8] Coumans FAW, Doggen CJM, Attard G, et al. All circulating EpCAM+CK+CD45- objects predict overall survival in castration-resistant prostate cancer. *Ann Oncol Off J Eur Soc Med Oncol.* [Internet]. 2010;21(9):1851–1857. Available from: <https://academic.oup.com/annonc/article-lookup/doi/10.1093/annonc/mdq030>
- [9] Nanou A, Coumans FAW, van Dalum G, et al. Circulating tumor cells, tumor-derived extracellular vesicles and plasma cytokeratins in castration-resistant prostate cancer patients. *Oncotarget.* [Internet]. 2018;9(27):19283–19293. Available from: <http://www.oncotarget.com/fulltext/25019>
- [10] Nanou A, Zeune LL, de Wit S, et al. Tumor-derived extracellular vesicles in blood of metastatic breast, colorectal, prostate and non-small cell lung cancer patients associate with worse survival [Internet]. In: *AACR 2019 Proceedings: Abstract 4464 - American Association for Cancer Research*, Atlanta, Georgia, USA; 2019 [cited 2019 May 27]. Available from: <https://books.google.nl/books?id=2CePDwAAQBAJ&pg=PT1982&lpg=PT1982&dq=Tumor-derived+extracellular+vesicles+in+blood+of+metastatic+breast,+colorectal,+prostate+and+non-small+cell+lung+cancer+patients+associate+with+worse+survival&source=bl&ots=qaCaW8WrEI&as>
- [11] Coumans F, van Dalum G, Terstappen LLWMM. CTC Technologies and Tools. *Cytom A.* 2018;93(12):1197–1201.
- [12] Kotrbová A, Štěpka K, Maška M, et al. TEM ExosomeAnalyzer: a computer-assisted software tool for quantitative evaluation of extracellular vesicles in transmission electron microscopy images. *J Extracell Vesicles.* 2019;8:1.
- [13] Zabeo D, Cvjetkovic A, Lässer C, et al. Exosomes purified from a single cell type have diverse morphology. *J Extracell Vesicles.* 2017;6:1.
- [14] van der Pol E, Coumans FAW, Grootemaat AE, et al. Particle size distribution of exosomes and microvesicles determined by transmission electron microscopy, flow cytometry, nanoparticle tracking analysis, and resistive pulse sensing. *J Thromb Haemost.* 2014;12(7):1182–1192.
- [15] Ramirez MI, Amorim MG, Gadelha C, et al. Technical challenges of working with extracellular vesicles. *Nanoscale* 2018;10(3), 881–906. Available from: <http://xlink.rsc.org/?DOI=C7NR08360B>
- [16] Gualerzi A, Kooijmans SAA, Niada S, et al. Raman spectroscopy as a quick tool to assess purity of extracellular vesicle preparations and predict their functionality. *J Extracell Vesicles.* [Internet]. 2019;8(1). Available from: <https://www.tandfonline.com/action/journalInformation?journalCode=zjev20>
- [17] Böing AN, van der Pol E, Grootemaat AE, et al. Single-step isolation of extracellular vesicles by size-exclusion chromatography. *J Extracell Vesicles.* [Internet]. 2014;3, 10.3402/jev.v3.23430. Available from: <http://www.ncbi.nlm.nih.gov/pubmed/25279113>
- [18] Van Der Pol E, van Gemert MJC, Sturk A, et al. Single vs. swarm detection of microparticles and exosomes by flow cytometry. *J Thromb Haemost.* [Internet]. 2012;10(5):919–930. Available from: <http://doi.wiley.com/10.1111/j.1538-7836.2012.04683.x>
- [19] van der Pol E, de Rond L, Coumans FAWW, et al. Absolute sizing and label-free identification of extracellular vesicles by flow cytometry. *Nanomedicine Nanotechnology, Biol Med.* [Internet]. 2018;14(3):801–810. Available from: <https://doi.org/10.1016/j.nano.2017.12.012>
- [20] Enciso-Martinez A, van der Pol E, Lenferink ATMM, et al. Synchronized Rayleigh and Raman scattering for the characterization of single optically trapped extracellular vesicles. *Nanomed Nanotechnol Biol Med.* [Internet]. 2019;24, 102109. Available from: <http://www.sciencedirect.com/science/article/pii/S1549963419301935>
- [21] Ashkin A. Acceleration and trapping of particles by radiation pressure. *Phys Rev Lett.* [Internet]. 1970;24(4):156–159. Available from: <https://journals.aps.org/prl/pdf/10.1103/PhysRevLett.24.156>
- [22] Ashkin A, Dziedzic JM, Chu S. Observation of a single-beam gradient force optical trap for dielectric particles. *Opt Lett.* [Internet]. 1986;11(5):288–290. Available from: https://www.osapublishing.org/DirectPDFAccess/C179D625-C7ED-5824-AC50C0B8F3390362_8652/ol-11-5-288.pdf?da=1&id=8652&seq=0&mobile=no
- [23] Penders J, Pence IJ, Horgan CC, et al. Single Particle Automated Raman Trapping Analysis. *Nat Commun.* [Internet]. 2018;9(1), 4256. Available from: <http://www.nature.com/articles/s41467-018-06397-6>
- [24] Kruglik SG, Royo F, Guigner J-M-M, et al. Raman tweezers microspectroscopy of circa 100 nm extracellular vesicles. *Nanoscale.* [Internet]. 2019;11(January), 1661–1679. Available from: <https://pubs.rsc.org/en/Content/ArticleLanding/2019/NR/C8NR04677H#!divAbstract>
- [25] Smith ZJ, Lee C, Rojalin T, et al. Single exosome study reveals subpopulations distributed among cell lines with variability related to membrane content (SI). *J Extracell Vesicles.* [Internet]. 2015;4(1), 28533. Available from: <http://www.ncbi.nlm.nih.gov/pubmed/26649679>
- [26] Lee W, Nanou A, Rikkert L, et al. Label-free prostate cancer detection by characterization of extracellular vesicles using raman spectroscopy. *Anal Chem.* [Internet]. 2018;90, 11. Available from: ;(). : <https://pubs.acs.org/sharingguidelines>
- [27] Benvenuto MA, Gordon IJ, Poppi DP, et al. Fast characterisation of cell-derived extracellular vesicles by nanoparticles tracking analysis, cryo-electron microscopy, and Raman tweezers microspectroscopy. *J Extracell Vesicles.*

- [Internet]. 2012;1 (1),229–238. Available from: <http://www.sciencedirect.com/science/article/pii/S1871141309002716>
- [28] Carney RP, Hazari S, Colquhoun M, *et al.* Multispectral optical tweezers for biochemical fingerprinting of CD9-positive exosome subpopulations. *Anal Chem.* [Internet]. 2017;89(10),5357–5363. Available from: <https://pubs.acs.org/doi/pdf/10.1021/acs.analchem.7b00017>
- [29] de Rond L, Coumans FAWW, Nieuwland R, *et al.* van der Pol E. Deriving extracellular vesicle size from scatter intensities measured by flow cytometry. *Curr Protoc Cytom.* 2018;86(1):e43.
- [30] de Rond L, Libregts SFWM, Rikkert LG, *et al.* Refractive index to evaluate staining specificity of extracellular vesicles by flow cytometry. *J Extracell Vesicles.* [Internet]. 2019;8 (1),1643671. Available from: <https://doi.org/10.1080/20013078.2019.1643671>
- [31] Uzunbajakava N, Lenferink A, Kraan Y, *et al.* Nonresonant confocal Raman imaging of DNA and protein distribution in apoptotic cells. *Biophys J.* [Internet]. 2003;84(6),3968–3981. Available from: <http://www.ncbi.nlm.nih.gov/pubmed/12770902>
- [32] Van Manen HJ, Uzunbajakava N, Van Bruggen R, *et al.* Resonance Raman imaging of the NADPH oxidase subunit cytochrome b 558 in single neutrophilic granulocytes. *J Am Chem Soc.* 2003;125(40):12112–12113.
- [33] Mätzler C MATLAB Functions for Mie Scattering and Absorption Version 2 [Internet]. Available from: http://www.atmo.arizona.edu/students/courselinks/spring09/atmo656b/maetzler_mie_v2.pdf.
- [34] Sultanova NG, Zlatarov BA, Sultanova N, *et al.* Dispersion Properties of Optical Polymers., 9. Available from: <https://www.researchgate.net/publication/234102654>.
- [35] Bass M, DeCusatis C, Enoch J, *et al.* Handbook of optics, third edition volume iv: optical properties of materials, nonlinear optics, quantum optics [Internet]. McGraw-Hill, Inc. Available from: <http://scholar.google.com/scholar?hl=en&btnG=Search&q=intitle:No+Title#0%5Cnhttp://books.google.ca/books?id=acrmuZpdSFEC>
- [36] Ning X, Selesnick IW, Duval L. Chromatogram baseline estimation and denoising using sparsity (BEADS). *Chemom Intell Lab Syst.* 2014;139:156–167.
- [37] Movasaghi Z, Rehman S, Rehman IU. Zanyar Movasaghi SR& DIUR. Raman spectroscopy of biological tissues. *Appl Spectrosc Rev.* [Internet]. 2007;42 (5),493–541. Available from: <http://www.tandfonline.com/action/journalInformation?journalCode=laps20>
- [38] Van Der Pol E, Coumans FAW, Sturk A, *et al.* Refractive Index Determination of Nanoparticles in Suspension Using Nanoparticle Tracking Analysis. *Nano Letters.* 2014;14(11):6195–6201. Available from: <http://pubs.acs.org/doi/10.1021/nl503371p>
- [39] De Rond L, van der Pol E, Hau CM, *et al.* Comparison of generic fluorescent markers for detection of extracellular vesicles by flow cytometry. *Clin Chem.* [Internet]. 2018;64(4),680–689. Available from: <http://www.ncbi.nlm.nih.gov/pubmed/29453194>
- [40] Aass HCD, Øvstebø R, A-MS T, *et al.* Fluorescent particles in the antibody solution result in false TF- and CD14-positive microparticles in flow cytometric analysis. *Cytom Part A.* [Internet]. 2011;79A(12), 990–999. Available from: <http://www.ncbi.nlm.nih.gov/pubmed/21990118>
- [41] Chan JW, Motton D, Rutledge JC, *et al.* Raman spectroscopic analysis of biochemical changes in individual triglyceride-rich lipoproteins in the pre-and postprandial state. 2005. Available from: <https://pubs.acs.org/sharingguidelines>
- [42] Wood BR, Caspers P, Puppels GJ, *et al.* Resonance Raman spectroscopy of red blood cells using near-infrared laser excitation. *Anal Bioanal Chem.* 2007;387(5):1691–1703.